IEEE Access
Multidisciplinary | Rapid Review | Open Access Journal

Received September 14, 2017, accepted November 21, 2017, date of publication December 6, 2017,
date of current version February 14, 2018.

Digital Object Identifier 10.1109/ACCESS.2017.2778193

Electromagnetic Needleless Injector With Halbach Array Towards Intravitreal Delivery

HONGLIANG REN[1,3], (Senior Member, IEEE), BOK SENG YEOW[1], JINJI SUN[1], AND JAYANT VENKATRAMANI IYER[2]

[1]Department of Biomedical Engineering, National University of Singapore, Singapore 117583
[2]Singapore Eye Research Center, Singapore General Hospital, Singapore 169608
[3]National University of Singapore Suzhou Research Institute, Suzhou 215123, China

Corresponding author: Hongliang Ren (ren@nus.edu.sg)

This work was supported in part by the Singapore Academic Research Fund, Magnetically Actuated Micro-Robotics, under Grant R-397-000-173-133, and in part by the National Natural Science Foundation of China NSFC under Grant 51405322.

ABSTRACT The fear of needles and pain prevents some patients from seeking intravitreal treatment, which drives our group to develop a needleless device for performing intravitreal injections. A prototype for an electro-magnetically actuated needleless injector, based on Halbach arrays, is described and characterized in a laboratory setting. The implication of the prototype for needleless ocular drug delivery is investigated. This investigation is intended to improve drug delivery of glaucoma medication with a safe needleless approach. We detail the design aspects of the injector and characterized the device with custom-made phantoms. It was observed that, despite delivering the drug bolus to the center, the viscous vitreous phantom indicated vorticities similar to counter rotating vortex pairs, which could cause damage to the retina. The observed peak velocity during the phantom experiments was 6.1 mm/sec at the retinal layer, indicating that the delivery bolus can impart shear forces to the retina via the vitreous.

INDEX TERMS Magnetic actuator, ocular drug delivery, Halbach, injector, intravitreal needleless injection.

I. INTRODUCTION

Intravitreal injections are used in treating ocular diseases, such as glaucoma, which develops from common diseases such as diabetes [1], systemic hypertension [2], or simply with aging [3]. Glaucoma (a chronic increase in intra-ocular pressure) increases the risk for vision loss where the damage is usually irreversible [4]. Glaucoma medication (Timolol, Betaxolol, Ecothiopate iodide, isoflurophate, Acetazolamide, Mannitol [5]) are delivered via eye-drops, tablets and injections to control the disease progression. Our scope is specific to the treatment of ocular hypertension (typically above 21 mmHg but is patient dependent) via intravitreal drug delivery [6]. Traditional treatment utilizes a 31-guage needle inserted a few millimeters posterior to the corneal limbus. The actual insertion distance is patient specific, but is located at the pars plana (anterior to the ora serrata) and angled into the center of the eye. From the patient's perspective, the benefits of a needleless approach is primarily circumventing needle phobia [7], additionally it could reduce pain and make the procedure easier to perform. Conventionally, local anesthetics (Amethocaine, Benoxinate and Proparacaine) are given to mitigate pain [5]. Further, there are reported benefits of a better drug dispersion profile [8], [9], which may improve drug delivery to the retina. However, the needleless approach should be demonstrated to not compromise safety over the conventional procedure. There exist a number of approaches for needleless drug delivery [10], which differentiates in the methods for accelerating the drug (fluid or particle) to a high velocity [11], [12] for penetration through a surface barrier. Generally, Bernoulli's principle is adopted and large volume of fluid is forced through a small orifice to achieve the high velocities; The small jet diameter and short injection time is the suggested ''evidence'' for reducing pain. Contrasting intra-ocular and transdermal [13] procedures, the injection emphasizes precision, avoiding possible damage to the retina [11]. It has been shown that electro-mechanical actuation can achieve a fine level of control [14]–[22] in real-time, which is useful for jet control after penetrating the sclera [23]; The delivery-jet has to slow down sufficiently to prevent damage to the retina and delivers medication to the precise depth [17]–[22]. Electromagnetism has also been demonstrated for use in controlled drug delivery

2169-3536 © 2017 IEEE. Translations and content mining are permitted for academic research only.
Personal use is also permitted, but republication/redistribution requires IEEE permission.
See http://www.ieee.org/publications_standards/publications/rights/index.html for more information.

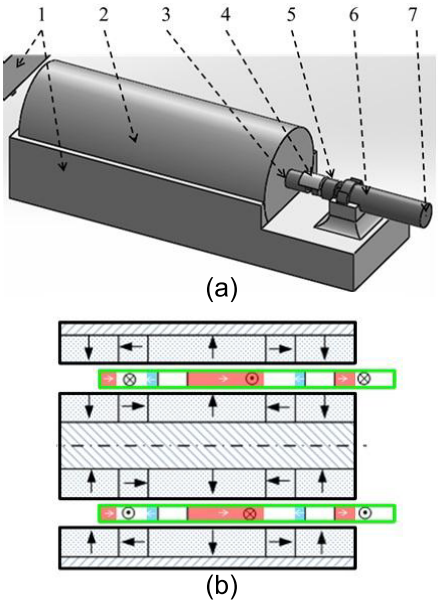

FIGURE 1. (a) - Elements of the Prototype Injector: (1) Casing, (2) Halbach actuator, (3) Actuator piston, (4) Connector for piston to plunger, (5) Plunger of ampoule, (6) Ampoule & (7) Orifice of Ampoule. (b) - Schematic of the Halbach actuator: elements with black arrows are permanent magnets, while the elements with encircled dots or crosses represent copper coils. The permanent magnets are fixed relative to each other, while the coils can move relative to the permanent magnets.

via the delivery of magnetic particles [24]–[26]. To further the research in magnetically actuated needle-free jet injectors, we propose a Halbach array inspired [27]–[29] actuator in this paper to investigate needleless intravitreal injections.

The primary contributions of the paper include,

1) The development of a novel actuator (Fig.1), with high current stiffness and passive regulation owing to the Halbach design. Higher current stiffness allows high force for scleral penetration while the passive feedback regulation limits large forces towards the end of the injection phase; This prevents potential damages to the retina.
2) Development of phantom models to visualize the injection phenomenon with our needleless Halbach injector. The phantom model allows us to capture the injection dynamics via Particle Image Velocimetry (PIV) to examine the safety aspects of a needleless drug delivery.
3) This prototype and lab-based proof of concept, investigates the safety concerns of such an approach such that the benefits of needleless technologies can be applied to intravitreal drug deliveries. We observed that while the injection delivers the injectant jet to the center of the eye there can still be damage to the retina. This indicates that further work to understand and dampen the vorticities is prudent if such an approach is to be commercialized.

II. MATERIALS AND METHODS

A. NEEDLELESS HALBACH INJECTOR PASSIVE REGULATION

The passive regulation is a consequence of the alternating magnetic field direction and coil current direction. During the initial injection phase, large forces for sclera penetration is required (Fig.2a&b); when current is applied, the Lorentz interactions between the wire currents and the magnetic fields results in mechanical motion. This motion is dependent on the interaction surface area, which reduces over the injection stroke; parallel magnetic fields as circled in orange do not contribute to the axial motion directly. The specific lengths of each section can be tailored to meet specific patient needs. Towards the end of the injection phase, the coil passes the parallel magnetic field region, where the coil is simultaneously experiencing opposing fields giving rise to antagonistic forces (Fig.2c). As the plunger displacement increases, the opposition forces increases thus dampening the motion. Adjustable fixation screws prematurely stop the plunger, allowing a reverse current to return the plunger back to the initial state. The implications of the passive feedback regulation changes the force constant over the injection stroke. The force constant of the injector (similar to a spring constant) represents the amount of force that the injector can produce for a given input current. The force constant is experimentally determined and the implication of such a model is exemplified via simulations. The force constant is fitted with a high order polynomial curve (Fig.3c), representing the transition from the blue circle to the orange circle (Fig.2b) and dampening (Fig.2c).

B. NEEDLELESS HALBACH INJECTOR SYSTEM

The block control diagram is shown (Fig.3a). When electrical current is supplied, interactions between the magnetic field (generated by the arrangement of permanent magnets) and the current in the coils generate a magnetic force. The wire coils move due the Lorentz forces and transfers the acceleration to the plunger. Subsequently, displacements of the ampoule, ejects fluid at the nozzle. Our injector system follows a similar control diagram to [20], converting an electrical signal to a mechanical output. In Fig.3a, (V_{olt}) refers to the input voltage to the actuator. (IRF) is the Impulse Response Filter [22]. (I) is the current running in the coils. (K) refers to the force constant of the actuator. (F) is the force exerted by the actuator on the plunger of the ampoule. A set of Ordinary Differential Equations (ODE) describes the coupling the mechanics between force, pressure and displacement. (P) is the pressure in the ampoule. (x) is the displacement of the actuator piston and ampoule plunger (we assume that they are synonymous). The Halbach design's passive feedback is a function of piston stroke position (x) and changes the actuator's force constant (K). Presently, this prototype has no active feedback control. (V_{jet}) is the velocity of the fluid at the ampoule orifice. The jet velocity (V_{jet}) will determine the penetration of the sclera and the injection profiles in the vitreous.

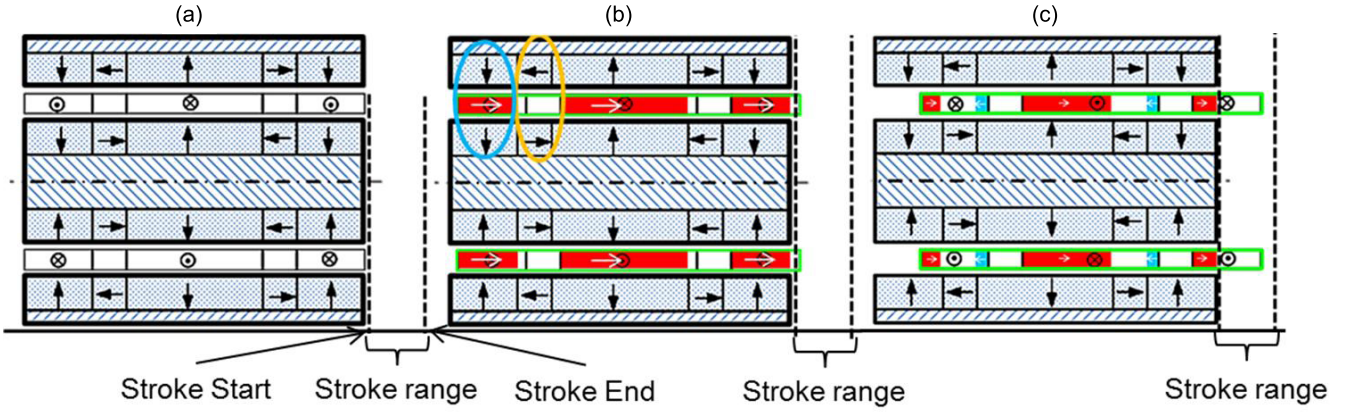

FIGURE 2. Illustration of the passive feedback mechanism. (a) Shows the arrangement of permanent magnets and wire coils in the actuator; black arrows indicate the magnetization direction of the permanent magnet, while a circle with a cross or dot indicate the wire coiling out of or into the plane. The red regions with white arrows indicate the Lorentz force driving the axial motion. The blue regions with white arrows indicate the Lorentz force dampening the motion by generating an opposition force. (b) Indicates the actuator at the initial injection phase requiring high force for sclera penetration; when current is applied, the Lorentz interactions between the wire currents and the magnetic fields causes the mechanical motion. This motion is a function of the interaction surface area, which reduces over the injection stroke, as parallel magnetic fields as circled in orange do not contribute to the axial motion directly. The specific lengths of each section can be tailored to the injection phase needs. (c) Illustrates the final delivery phase into vitreous where the passive feedback kicks in to reduce forces. As the coil passes the parallel magnetic field region, the coil is simultaneously experiencing opposing fields giving rise to antagonistic forces. As the displacement of the plunger increases, the forces opposing the motion increases. Adjustable fixation screws prematurely stop the plunger, allowing a reverse current to return the plunger back to the initial state.

C. NEEDLELESS HALBACH INJECTOR FORCE CONSTANT

To characterize the force response of the Halbach actuator, we measured the impact force of the actuator at prescribed stroke-lengths (actuation stroke of 5 mm corresponds to a delivery dosage of about 50 μL) for a given unit-step input. The experimental set-up is as shown (Fig.3b). The results concur with predicted rapid decrease in the force-current response across the stroke (Fig.3c). Two different voltage points were tested to confirm that results are a function of the actuator properties and not due to input voltage used. We tested at 12 V and 17.5 V, which corresponds to 1.1 A and 1.6 A steady state current. The current stiffness at different voltages are comparable (On average, there is 6.2% difference) suggesting that it is a property of the injector. The maximum current stiffness value occurs at the start of the actuation and is 12.96 $\mathrm{N} \cdot \mathrm{A}^{-1}$ while the average is 6.91 $\mathrm{N} \cdot \mathrm{A}^{-1}$. The third order polynomial fit has a Sum of Squared Residuals value of, $\mathrm{R}^2 = 0.9923$.

D. NEEDLELESS HALBACH INJECTOR BULK MODULUS

The bulk modulus is a key parameter for the dynamics of the injection, especially for the initial high loading [22], [30]. Following the protocols outlined in [22], we measured the combined bulk modulus of the ampoule at various injectant volumes (50 μL, 150 μL, 200 μL). Volumes less than 50 μL were not tested, as we were unable to accurately determine the volume in the ampoule. The orifice of the ampoule was sealed with epoxy to prevent fluid from leaving the ampoule. The force and displacements were recorded and converted to pressure and volumetric changes. The bulk modulus (B) is defined in equation (1) relating pressure to volume changes.

$$B = V\frac{dP}{dV} \tag{1}$$

TABLE 1. Parameters for the simulation.

Symbol	Definition	Value
B	Combined Bulk Modulus (Pa)	$B = B_1(v) + B_2$
B_1	Component Bulk Modulus (Pa/m)	10009*
B_2	Component Bulk Modulus (Pa)	0.9366*
a_o	Cross-sectional area ampoule orifice (m^2)	$1.13e^{-8}$
a_p	Cross-sectional area Piston (m^2)	$2.83e^{-5}$
$\rho(rho)$	Density ($kg{\cdot}m^{-3}$)	1000
l	Maximum stroke length (m)	$5e^{-3}$
m_p	Piston mass (Kg)	0.05**
μ	Friction coefficient	0.24**
a_c	Contact surface area (m^2)	$1.13e^{-4}$
f_1	Model Constant ($N{\cdot}m^{-3}$)	722559515
f_2	Model Constant ($N{\cdot}m^{-2}$)	4813216
f_3	Model Constant ($N{\cdot}m^{-1}$)	15430
f_4	Model Constant (N)	1.82

* These values can be derived from the fit of Fig.3c.
**Taken from [17].

Our results indicate the bulk modulus is a linear relationship as shown in (Fig.3e); we have excluded the preloading region in the model. Our combined bulk modulus follows the simple linear equation where the Sum of Squared Residuals value, $\mathrm{R}^2 = 0.993$. The relationship between the bulk modulus and the ampoule volume is used in the ODE model.

E. NEEDLELESS HALBACH INJECTOR ODE

We modified existing ODE models [17], [23] to represent our injector, equations (2), (3) & (4), where (P) is the pressure, (V) and (X) is the velocity and displacement of the plunger, the other symbols are defined in Table.1.

$$\dot{\mathrm{P}} = \frac{V(B+P) - (b\sqrt{\frac{2P}{\rho}} \cdot \frac{a_o}{a_p})}{(L-X)} \tag{2}$$

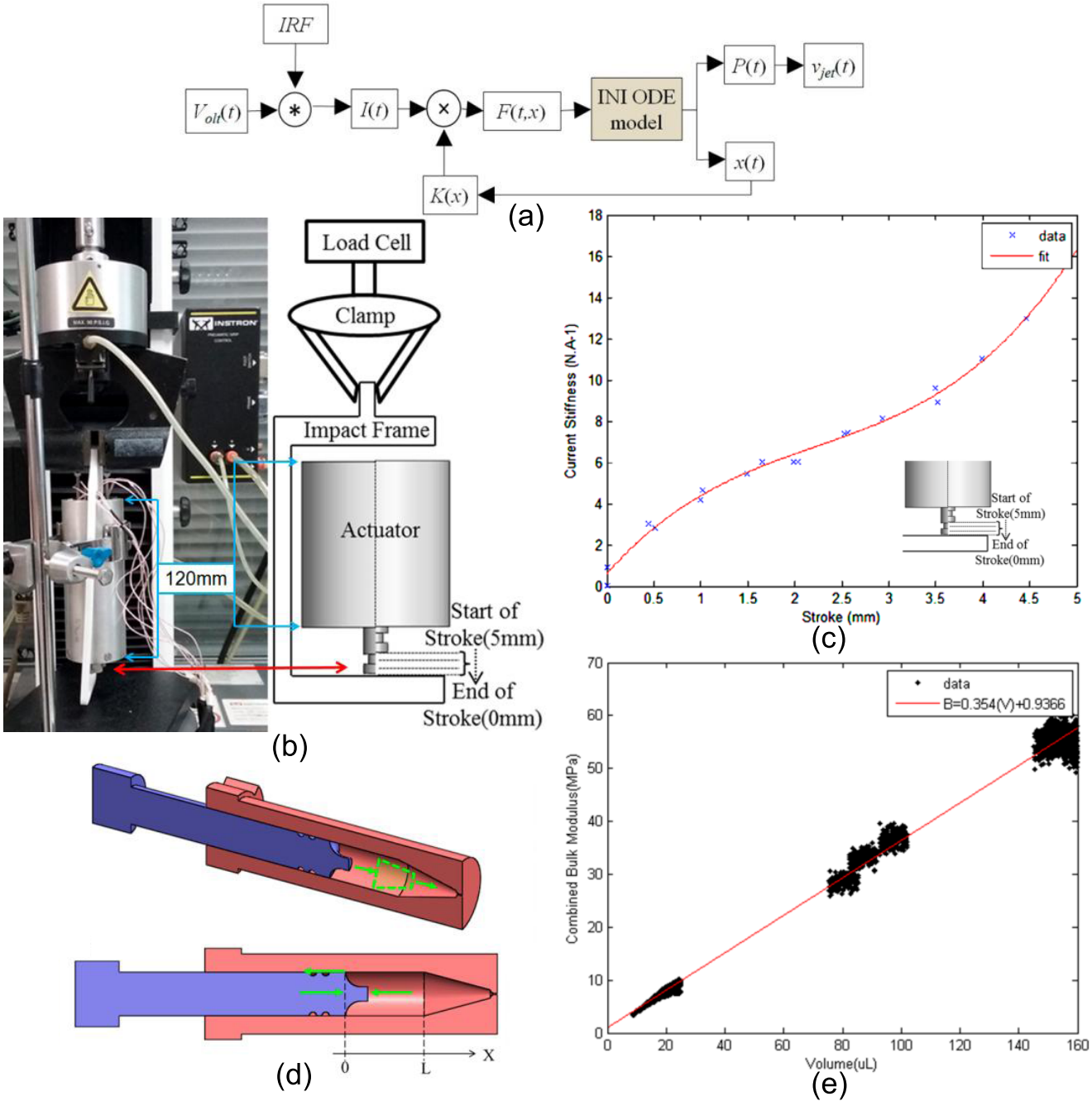

FIGURE 3. (a) Block diagram of the injection system. (b) Experimental set-up for force constant measurement with Instron 5940 Single Column Tabletop Model 1 kN. (c) Force constant results.The stroke of 5 mm is the start of the stroke and 0 mm is the end, one can visualize the plunger extending from the right (fully retracted) to left (fully extended) of the graph. (d) Free Body Diagram representation of the equations. The blue element represents the plunger and the red element represents the ampoule. (e) A linear fit to the change in pressure of the system due to compression.

$$\dot{V} = \frac{F_{EM} - (a_p + \mu a_c)}{m_p} \tag{3}$$

$$\dot{X} = V \tag{4}$$

In addition, the equation for the input force F_{EM} is given as the polynomial fit to (Fig.3c) at an input current of 3A.

$$F_{EM} = f_1 \cdot (l - x)^3 + f_2 \cdot (l - x)^2 + f_3 \cdot (l - x) + f_4 \tag{5}$$

The set of ODE equations is solved in MATLAB based on an iterative Runge-Kutta-4 solver. Relative tolerance was set at 10^{-5} and absolute tolerance set at 10^{-6}, time step of 10^{-4} sec and the total simulation time is 0.2 sec. We have modified the combined bulk modulus (B) to be a function of displacement as per Fig.3e. The model simulates the Pressure in the ampoule (P) and the Displacement of the plunger (x). (Fig.3d) is a pictorial representation for equations 2, 3 & 4.

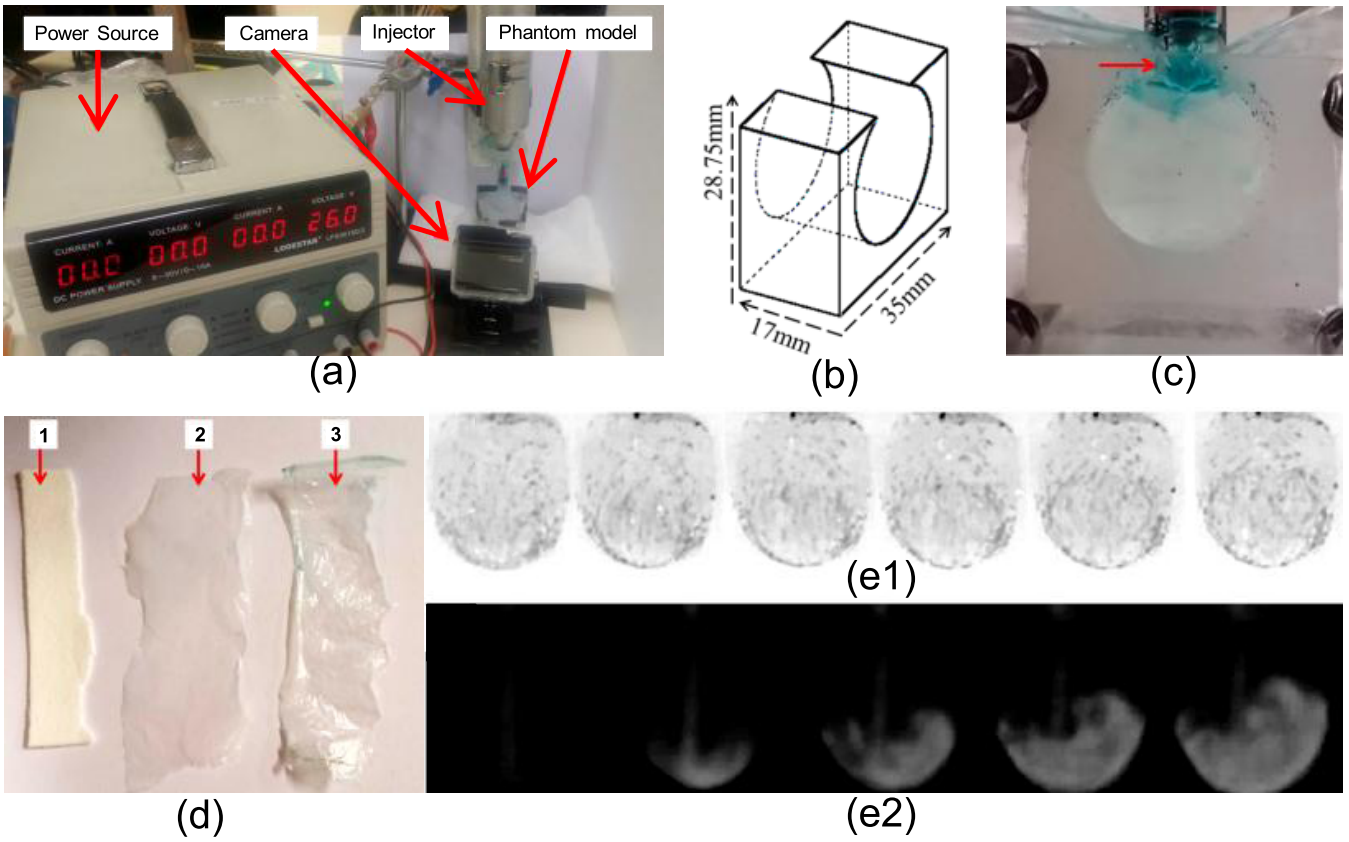

FIGURE 4. (a) Experimental Set-up. (b) Dimensions of the phantom. (c) The red arrow indicates the scleral membrane. (d) Thickness of (d1) = 0.8 mm; (d2) = 0.2 mm; (d3) = 0.1 mm. (e) Post Processed Time-lapse images of injection at 30 V without a barrier, (e1) - Seeding particles, (e2) - Dyed injectant.

As the plunger moves at a particular velocity, the fluid in the ampoule is compressed leading to an increase in pressure of the control volume. The increase in pressure is comprised of the displaced volume from the plunger and the compressed volume by the plunger. Pressure loss in the control volume is due to fluid volume escaping via the nozzle. From [30], the Velocity of the fluid at the nozzle is rewritten in equation 2 as

$$V_{jet} = \sqrt{\frac{2P}{\rho}} \tag{6}$$

The simulation results agree with the initial oscillatory patterns observed by [22] and [30] due to the reflection of the compression waves. Various polynomial orders to Fig.3c are tested and compared (Section III-A).

F. VITREOUS CHAMBER EXPERIMENTAL SET-UP

The set-up (Fig.4a) consists of the electromagnetic injector held in place by a retort stand with a clamp. The camera (GoPro Hero4) captures images at 30 fps, at a resolution of 1080p. Image frames are extracted using GoPro Studio and further processed in MATLAB. To visualize the flow, we seeded the vitreous with reflective particles (Fig.4e1) and used a dyed injectant (Fig.4e2). The vitreous chamber is modeled as a cylinder instead of a sphere to allow a non-distorted view into the chamber. Dimensions of the orbit for simulations have been reported previously [14], [31], [32], and we have opted to use a cylinder of 25 mm in diameter and 17 mm in length. This relates to an orbital 25 mm in diameter and a volume of around 8 mL. We are using an injection volume of 50 uL, which is a common injection volume. The vitreous is modeled with alginate dissolved in water and the concentration set such that the eventual viscosity of the solution is around 4000 cP [33]. This model is simple and does not capture the intricacies [34] of the vitreous but is sufficient for this initial phase of testing. The vitreous is housed in a silicon mould, which is in turn clamped between two clear 1.5 mm acrylic sheets. The model has a 10.9 mm by 17 mm rectangular opening where we can mount the phantom sclera and fill the vitreous cavity (Fig.4b). The sclera barrier is simulated with Poly-CaproLactone (PCL) as suggested by [30] (Fig.4c&d). Our sclera phantom is not as hard or tough as the actual sclera [29]–[34], but was still able to serves as a penetration resistant membrane layer. We tested 0.8 mm PCL expanded with Calcium Carbonate, a 0.2 mm and 0.1 mm thick PCL-only barrier. Other membrane layers, (choroid and conjunctiva) are assumed negligible with respect to the sclera. The injector at higher voltages, above 50 V, penetrates biological tissue such as excised

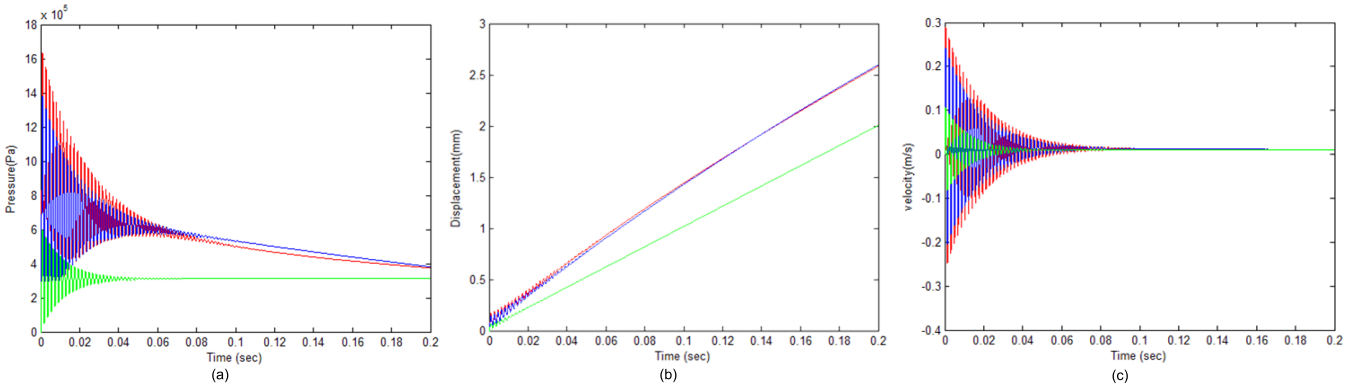

FIGURE 5. The red graph represents the third order fit. The blue graph represents the first order fit. The green graph represents the zero order fit. (a) shows the pressure profiles over time, (b) and (c) shows displacement and velocity respectively. The third order model is able to achieve higher initial pressures and decays at a faster rate, which benefits control to reducing the jet velocities at later stages of the injection.

chicken skin. Due to safety limitations the subsequent experimental results were collected strictly under 30 V.

G. PARTICLE IMAGE VELOCIMETRY

We utilized the open source PIV toolbox, PIVlab [40]–[42]. The primary methodology used is direct cross correlation (DCC). The DCC method takes the peak in the correlation matrix (C(m, n)) as the most likely solution for the velocity (i, j) map at (m,n).

$$\mathrm{C(m,\,n)} = \sum_{i}\sum_{j} A(i,j)B(i-m,j-n) \tag{7}$$

This method requires seeding particles (Fig.4e1) such that features from the previous frame can be contrasted with the current frame. The benefit of this method is the visualization of flow, while dye injectant can indicate the bulk position of drug. Ideally, the injection process should not disturb the vitreous situated near the retina. Prior to analysis, a contrast filter is used to enhance the detection with a RGB threshold filter.

III. RESULTS

A. ODE SIMULATION VARYING F_{EM} POLYNOMIALS

The ODE simulation is explored by using the data points from (Fig.3c); the third, first and zero order polynomials are obtained by the least squared regression. The third order fit (which is the current model of the injector) represents the influence of the passive feedback dampening, exemplifying the case of a unit step impulse to our device (Fig.5 red line). The physical interpretation of the first order model would be the case of a solenoid, but with a linearly decreasing current input (Fig.5 blue line). The zero order model would be the case if the current was not decreased and the actuator had a constant force value (Fig.5 green line). The passive feedback allows for both, a higher pressure generation at the start and a faster decay as indicated around the 0.06 second mark. Simulation results (Fig.5), indicates that the higher order polynomial is able to achieve a higher injecting pressure and faster pressure decay rate.

B. INFLUENCE OF SCLERAL BARRIER

We tested 4 barrier conditions: no barrier, 0.1 mm barrier, 0.2 mm barrier and 0.8 mm barrier, (Fig.6). The input voltage is 30 volts and there is a standardized 1 mm gap between the ampoule orifice and the membrane. Without a membrane, the injectant reaches the back of the phantom and as we increase the thickness (resistance) of the barrier; changes to the delivery depth is observed. Without resistance, the dispersion profile follows patterns similar to [13] and with resistance follows [38]. We further analyzed results from 0.1 mm membrane condition. The velocity magnitudes were greatest during the entry phase and peak observed was at 0.985 pix/frame = 3.8 mm/sec, (Fig.6b). The conversion, 1 pix $\approx$ 0.13 mm, is based on an average of 187.3 pix $\pm$ 1.874pix corresponding to a 25 mm fiducial marker and each frame takes 1/30 sec. The velocity peak occurs when fluid reaches maximum vertical displacement, typically transitioning from frame 1/30 to 2/30. The time resolution of these results can be further improved with better equipment. The corresponding velocity magnitude at the retina for each time frame is shown (Fig.6c). For frame 2 (Fig.6c green line) the Maximum Velocity = 0.985 pix/frame (3.8 mm/sec) and Average Velocity = 0.47 pix/frame (1.8 mm/sec) with a standard deviation = 0.202 pix/frame (0.8 mm/sec). During the high velocity phase, the velocities near the medial and lateral retinal walls experience the greatest velocity magnitudes. The shears from the initial jet and the geometries are suspected to give rise to transient eddy currents where the energy is dissipated. From (Fig.6c), it is suggested that the greatest velocity magnitudes occur along the retinal circumference and does not occur at the point of injection.

C. VARYING VOLTAGE

The effects of voltage variations on penetration depth are observed. To achieve drug delivery to the center of the eye, the voltage for the delivery phase is dependent on the viscosity of the injectant and the medium (vitreous). Tested voltages ranged between 14 V to 20 V; voltage outside this range leads to either a lack of actuation or excessive penetration

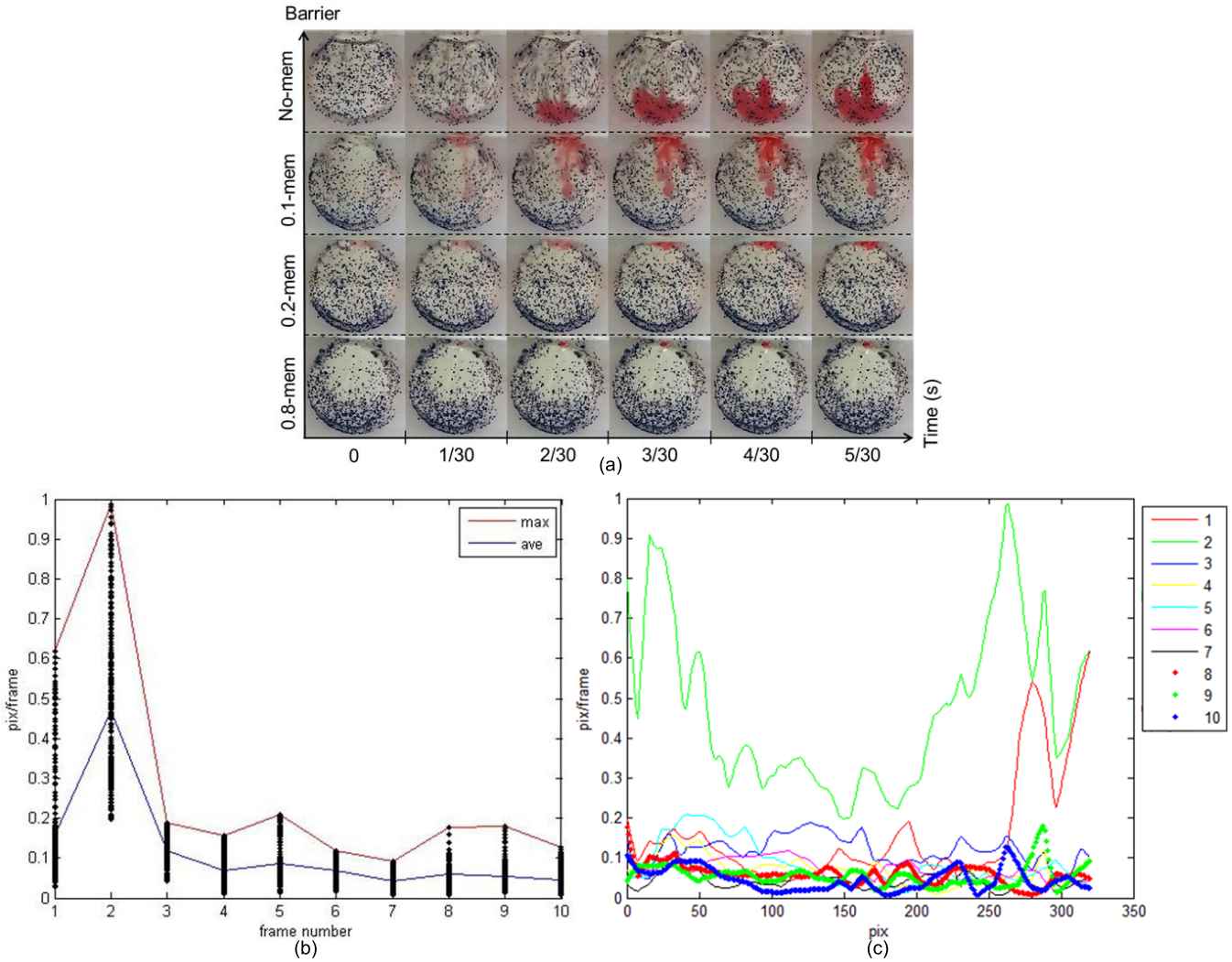

FIGURE 6. **(a) Dyed Injectant Frames at 30 V with varying penetration, where 0.1, 0.2, 0.8 mem refers to the thickness of the penetration barrier. (b) Velocity magnitudes over time frames. The blue lines traces the average data point values while the red line traces the maximum data point values. (c) Velocity magnitudes along the retinal circumference. Legend indicates the sequence of frames where red line 1 is the first frame and blue dot 10 is the last frame.**

depth. In general, an increase in voltage will increase the penetration depth and the dispersion of the fluid profile, (Fig.7a). Comparing the 15 V and 16 V velocity magnitudes at the various frames utilizing PIV, (Fig.7b&c); it is observed that a small change in input can have significant difference (31.3% increase in of peak velocities) near the retinal layer. The peak of the 16 V input is 1.57 pix/frame (6.1 mm/sec), at 15 V it is 0.81 pix/frame (3.2 mm/sec). The average for 16 V is 0.57 pix/frame (2.2 mm/sec) and at 15 V is 0.43 pix/frame (1.7 mm/sec). The peak of 16 V occurs earlier than 15 V by about 2 frames (67 mSec).

D. JET FORCE MEASUREMENTS

A force torque sensor (ATI nano17) was used to measure the impact force of the jet in the vitreous phantom at various depths (35 mm, 30 mm, 25 mm & 20 mm). The outer diameter of the acrylic cylinder is 25 mm and the wall thickness is 2 mm. The voltage is tested at 15 V and 20 V. The parameters of concern are the compressive force in the normal direction to the sensor surface (F_z) and the magnitude of the force vector ($Mag, Mag^2 = F(x)^2 + F(y)^2 + F(z)^2$). Comparison between the four depths did not have significant differences, contrary to our expectations. The 20 V input indicates higher F_z than the 15 V. From the *Mag* plot it is observed that there are significant force components in the other directions possibly due to the increased eddy shears at low voltages.

IV. DISCUSSION

Through our prototype we observed that, even though the bulk volume of the drug is delivered to the center of the vitreous, there can be energy diffusion from the injectant to the vitreous, translating into a velocity component near the retinal layer. This is clinically relevant as the shear forces can aggravate retinal detachment, (Fig.8b&c).

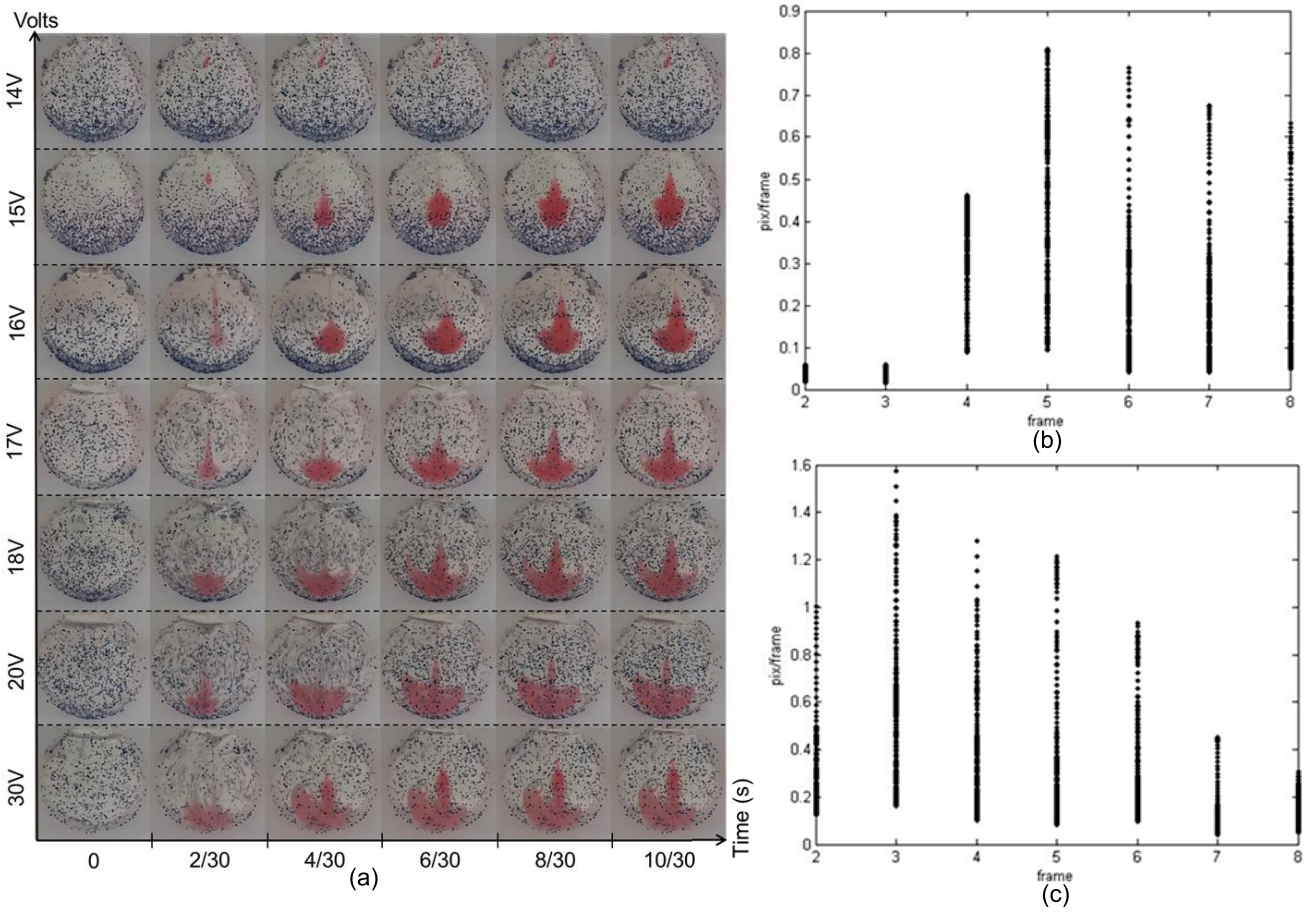

FIGURE 7. (a) Penetration Profile as a function of Voltage. 15 Volts and 16 Volts have the delivery bolus at the center of the prototype. (b) shows the velocities at the retinal circumference for an input of 15 Volts. (c) shows the velocities at the retinal circumference for an input of 16 Volts. Contrasting (b) and (c), the increase in voltage increases the magnitude of velocities.

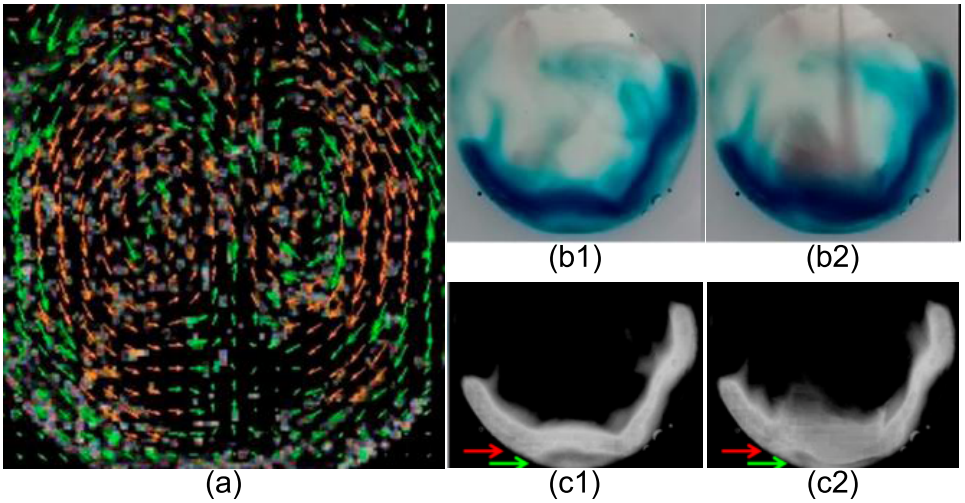

FIGURE 8. (a) The particle motion indicating the vortex observed. (b) For patients with detachment of the macular, caution is advised for a needleless approach where detachment can be aggravated. We simulate here the movement of an alginate sheet. (c) The image enhancement of (b) to better show motion from the green arrow to the red arrow.

To facilitate discussion, we adopt terminology from [15] to describe the injection delivery phases (after penetrating the sclera). (1) Reaching maximum injection depth, (2) injectant dispersion at maximum depth and (3) dispersion throughout the bolus volume. Additionally, phase (1) induces vorticities [44] shearing fluid posteriorly during phases (2&3),

(Fig.8A). This affects the final bolus profile of the injectant in the vitreous. The effects of injection voltage contribute to the velocities observed in (Fig.7) and are likely due to the fluidic eddies [45]. A small change in the voltage (15 V, 16 V) affects the penetration depth of the injectant and the profile of the injectant. Increasing the voltage delays the onset of phase (3). From force measurements at (15 V & 20 V), the phases in concern are different. At 20 V, phase (1) delivers the greatest force while at lower voltages, which are more applicable to drug delivery, the forces are delayed and spread out over various component directions. This indicates that shear forces should be looked into with greater concern. Analysis into the PIV slices support the notion where the greatest velocity magnitudes do not occur at point of injection but rather surrounding it, (Fig.6c). If we assume retinal attachment pressure to be 476 Pa [14] and a contact area of 10 mm disc, the sustainable force is 0.0374 N. From the test in Section III-D at 15 V the peak force was below 0.02 N, indicating that there is still a possibility of device implementation. Scleral thickness plays a significant role in the penetration mechanics. Given the huge variability in patient sclera for both thickness and failure thresholds, it appears unlikely that a simple feedback controller can accurately determine the injection depth after penetrating the sclera layer. To address this challenge, the resistance of the sclera must be further accounted for in the model or further tracking of the injectant bolus will be necessary to control the penetration depth.

V. CONCLUSION

We have designed a Halbach array based magnetic actuator for needleless intravitreal injections. The Halbach design has passive feedback, which reduces the force constant over the injection stroke (Fig.2&3c), which helps to decelerate the injectant and prevent retina damage. The injector has a high current stiffness ($12.96\ \mathrm{N} \cdot A^{-1}$) at the start of the injection stroke, which is necessary for injectant acceleration to penetrate the sclera. We fabricated an injection phantom, which allowed visualization of the injection dynamics (Fig.4) to better understand the delivery event. The results are processed with PIV to analyze the velocity fields during injection where we experimented with three variables relevant to needleless intravitreal drug delivery (Fig.6&7, Section III-D). We observed that the effects of scleral thickness as a penetration barrier cannot be ignored as it does affect penetration depth. Shearing forces and velocities proximal to the maximum injection depth should be further analyzed for future clinical applications of the device.

ACKNOWLEDGMENT

The authors would like to thank Mavis Yee Qin Ying for assisting with the data collection. *(Hongliang Ren and Bok Seng Yeow contributed equally to this work.)*

REFERENCES

[1] P. Rajeevan and K. Mahadevan, "A randomized clinical trial comparing efficacy of vitrectomy with intra vitreal triamcinolone acetonide injection and simple vitrectomy in patients with vitreous haemorrhage due to proliferative diabetic retinopathy," *J. Evol. Med. Dental Sci.*, vol. 2, no. 21, pp. 3778–3783, 2013.

[2] M. J. S. Langman, R. J. Lancashire, K. K. Cheng, and P. M. Stewart, "Systemic hypertension and glaucoma: Mechanisms in common and co-occurrence," *Brit. J. Ophthalmol.*, vol. 89, no. 8, pp. 960–963, 2005.

[3] H. A. Quigley, "Number of people with glaucoma worldwide," *Brit. J. Ophthalmol.*, vol. 80, no. 5, pp. 389–393, 1996.

[4] E. Lavik, M. H. Kuehn, and Y. H. Kwon, "Novel drug delivery systems for glaucoma," *Eye*, vol. 25, no. 5, pp. 578–586, 2011.

[5] R. W. Johnson and F. C. Forrest, *Local and General Anaesthesia for Ophthalmic Surgery*, 1st ed. Oxford, U.K.: Butterworth-Heinemann, 1994.

[6] J. O. Mason, III, P. A. Nixon, and M. F. White, "Intravitreal injection of bevacizumab (Avastin) as adjunctive treatment of proliferative diabetic retinopathy," *Amer. J. Ophthalmol.*, vol. 142, no. 4, pp. 685–688, 2006.

[7] P. Chua, "Evaluating patient discomfort, anxiety, and fear before and after ranibizumab intravitreous injection for wet age-related macular degeneration," *Arch. Ophthalmol.*, vol. 127, no. 7, pp. 936–945, 2009.

[8] T. M. Grant, K. D. Stockwell, J. B. Morrison, and D. D. Mann, "Effect of injection pressure and fluid volume and density on the jet dispersion pattern of needle-free injection devices," *Biosyst. Eng.*, vol. 138, pp. 59–64, Oct. 2015.

[9] Health & Medicine Week. (Nov. 2011). *Needle Free Vaccine Delivery—Technology Market Penetration and Roadmapping—Needle-Free Vaccine Delivery Technology Blazes the Path to Better Immunity Against Diseases and Pandemics*, Academic OneFile, p. 1824. Accessed: Dec. 6, 2017. [Online]. Available: link.galegroup.com.libproxy1.nus.edu.sg/apps/doc/A271715975/AONE?u=nuslib&sid=AONE&xid=f88ce255

[10] S. Swain, S. Beg, A. Singh, C. N. Patro, and M. E. Bhanoji Rao, "Advanced techniques for penetration enhancement in transdermal drug delivery system," *Current Drug Del.*, vol. 8, no. 4, pp. 456–473, 2011, doi: 10.2174/156720111795767979.

[11] E. L. Giudice and J. D. Campbell, "Needle-free vaccine delivery," *Adv. Drug Del. Rev.*, vol. 58, no. 1, pp. 68–89, 2006.

[12] J. C. Stachowiak, M. G. von Muhlen, T. H. Li, L. Jalilian, S. H. Parekh, and D. A. Fletcher, "Piezoelectric control of needle-free transdermal drug delivery," *J. Control. Release*, vol. 124, nos. 1–2, pp. 88–97, 2007, doi: 10.1016/j.jconrel.2007.08.017.

[13] G. Cevc and U. Vierl, "Nanotechnology and the transdermal route: A state of the art review and critical appraisal," *J. Control. Release*, vol. 141, no. 3, pp. 277–299, 2010, doi: 10.1016/j.jconrel.2009.10.016.

[14] X. Liu, L. Wang, C. Wang, G. Sun, S. Liu, and Y. Fan, "Mechanism of traumatic retinal detachment in blunt impact: A finite element study," *J. Biomech.*, vol. 46, no. 7, pp. 1321–1327, 2013.

[15] J. C. Stachowiak, T. H. Li, A. Arora, S. Mitragotri, and D. A. Fletcher, "Dynamic control of needle-free jet injection," *J. Control. Release*, vol. 135, no. 2, pp. 104–112, 2009.

[16] A. Schoubben *et al.*, "Dynamic behavior of a spring-powered micronozzle needle-free injector," *Int. J. Pharmaceutics*, vol. 491, nos. 1–2, pp. 91–98, 2015.

[17] A. Taberner, N. C. Hogan, and I. W. Hunter, "Needle-free jet injection using real-time controlled linear Lorentz-force actuators," *Med. Eng. Phys.*, vol. 34, no. 9, pp. 1228–1235, 2012.

[18] B. D. Hemond, A. Taberner, C. Hogan, B. Crane, and I. W. Hunter, "Development and performance of a controllable autoloading needle-free jet injector," *J. Med. Devices*, vol. 5, no. 1, p. 015001, 2011.

[19] B. D. Hemond, D. M. Wendell, N. C. Hogan, A. J. Taberner, and I. W. Hunter, "A Lorentz-force actuated autoloading needle-free injector," in *Proc. Int. Conf. IEEE Eng. Med. Biol. Soc.*, Aug./Sep. 2006, pp. 679–682.

[20] A. J. Taberner, N. B. Ball, N. C. Hogan, and I. W. Hunter, "A portable needle-free jet injector based on a custom high power-density voice-coil actuator," in *Proc. Int. Conf. IEEE Eng. Med. Biol. Soc.*, Aug./Sep. 2006, pp. 5001–5004.

[21] R. M. J. Williams, N. C. Hogan, P. M. F. Nielsen, I. W. Hunter, and A. J. Taberner, "A computational model of a controllable needle-free jet injector," in *Proc. Annu. Int. Conf. IEEE Eng. Med. Biol. Soc.*, Aug./Sep. 2012, pp. 2052–2055.

[22] R. M. J. Williams, B. P. Ruddy, N. C. Hogan, I. W. Hunter, P. M. F. Nielsen, and A. J. Taberner, "Analysis of moving-coil actuator jet injectors for viscous fluids," *IEEE Trans. Biomed. Eng.*, vol. 63, no. 6, pp. 1099–1106, Jun. 2016.
[23] J. S. Pulido, M. E. Zobitz, and K.-N. An, "Scleral penetration force requirements for commonly used intravitreal needles," *Eye*, vol. 21, no. 9, pp. 1210–1211, 2006.
[24] L. C. Barnsley, D. Carugo, M. Aron, and E. Stride, "Understanding the dynamics of superparamagnetic particles under the influence of high field gradient arrays," *Phys. Med. Biol.*, vol. 62, no. 6, pp. 2333–2360, 2017.
[25] A. Krafčík, P. Babinec, and I. Frollo, "Computational analysis of magnetic field induced deposition of magnetic particles in lung alveolus in comparison to deposition produced with viscous drag and gravitational force," *J. Magn. Magn. Mater.*, vol. 380, pp. 46–53, Apr. 2014.
[26] P. Babinec, A. Krafčík, M. Babincová, and J. Rosenecker, "Dynamics of magnetic particles in cylindrical Halbach array: Implications for magnetic cell separation and drug targeting," *Med. Biol. Eng. Comput.*, vol. 48, no. 8, pp. 745–753, 2010.
[27] Y. You, Y. Guo, S. Xiao, S. Yu, H. Ji, and X. Luo, "Numerical simulation and performance improvement of a multi-polar concentric Halbach cylindrical magnet for magnetic refrigeration," *J. Magn. Magn. Mater.*, vol. 405, pp. 231–237, May 2016.
[28] R. Bjørk, C. R. H. Bahl, A. Smith, D. V. Christensen, and N. Pryds, "An optimized magnet for magnetic refrigeration," *J. Magn. Magn. Mater.*, vol. 322, no. 21, pp. 3324–3328, 2010.
[29] R. Bjørk, A. Smith, and C. R. H. Bahl, "Analysis of the magnetic field, force, and torque for two-dimensional Halbach cylinders," *J. Magn. Magn. Mater.*, vol. 322, no. 1, pp. 133–141, 2010.
[30] A. B. Baker and J. E. Sanders, "Fluid mechanics analysis of a spring-loaded jet injector," *IEEE Trans. Biomed. Eng.*, vol. 46, no. 2, pp. 235–242, Feb. 1999.
[31] A. A. Weaver, E. A. Kennedy, S. M. Duma, and J. D. Stitzel, "Evaluation of different projectiles in matched experimental eye impact simulations," *J. Biomech. Eng.*, vol. 133, no. 3, p. 031002, 2011.
[32] A. A. Weaver, K. L. Loftis, J. C. Tan, S. M. Duma, and J. D. Stitzel, "CT based three-dimensional measurement of orbit and eye anthropometry," *Invest. Opthalmol. Vis. Sci.*, vol. 51, no. 10, pp. 4892–4897, 2010.
[33] G. Fogli *et al.*, "New eye phantom for ophthalmic surgery," *J. Biomed. Opt.*, vol. 19, no. 6, p. 068001, 2014.
[34] P. S. Kashani. (2012). Biomechanics of vitreous gel (Order No. 3532477). ProQuest Dissertations & Theses Global. [Online]. Available: http://libproxy1.nus.edu.sg/login?url=https://search-proquest-com.libproxy1.nus.edu.sg/docview/1163738886?accountid=13876
[35] J. A. Bisplinghoff, C. McNally, S. J. Manoogian, and S. M. Duma, "Dynamic material properties of the human sclera," *J. Biomech.*, vol. 42, no. 10, pp. 1493–1497, 2009.
[36] R. E. Norman *et al.*, "Dimensions of the human sclera: Thickness measurement and regional changes with axial length," *Experim. Eye Res.*, vol. 90, no. 2, pp. 277–284, 2010.
[37] T. W. Olsen, S. Y. Aaberg, D. H. Geroski, and H. F. Edelhauser, "Human sclera: Thickness and surface area," *Amer. J. Ophthalmol.*, vol. 125, no. 2, pp. 237–241, 1998.
[38] A. Elsheikh, B. Geraghty, D. Alhasso, J. Knappett, M. Campanelli, and P. Rama, "Regional variation in the biomechanical properties of the human sclera," *Experim. Eye Res.*, vol. 90, no. 5, pp. 624–633, 2010.
[39] S. L.-Y. Woo, A. S. Kobayashi, W. A. Schlegel, and C. Lawrence, "Nonlinear material properties of intact cornea and sclera," *Experim. Eye Res.*, vol. 14, no. 1, pp. 29–39, 1972.
[40] W. Thielicke and E. J. Stamhuis, "PIVlab—Towards user-friendly, affordable and accurate digital particle image velocimetry in MATLAB," *J. Open Res. Software*, vol. 2, no. 1, p. e30, 2014, doi: http://doi.org/10.5334/jors.bl.
[41] T. William and J. Eize. (2016). PIVlab—Time-resolved digital particle image velocimetry tool for MATLAB. figshare. [Online]. Available: http://dx.doi.org/10.6084/m9.figshare.1092508
[42] W. Thielicke, *The Flapping Flight of Birds: Analysis and Application*. Groningen, The Netherlands: University of Groningen, 2014.
[43] J. Schramm-Baxter, J. Katrencik, and S. Mitragotri, "Jet injection into polyacrylamide gels: Investigation of jet injection mechanics," *J. Biomech.*, vol. 37, no. 8, pp. 1181–1188, 2004.
[44] J. C. Stachowiak, D. L. Richmond, T. H. Li, A. P. Liu, S. H. Parekh, and D. A. Fletcher, "Unilamellar vesicle formation and encapsulation by microfluidic jetting," *Proc. Nat. Acad. Sci. USA*, vol. 105, no. 12, pp. 4697–4702, 2008, doi: 10.1073/pnas.0710875105.
[45] T. Maxworthy, "The structure and stability of vortex rings," *J. Fluid Mech.*, vol. 51, no. 1, pp. 15–32, 1972, doi: 10.1017/S0022112072001041.

HONGLIANG REN received the Ph.D. degree in electronic engineering from the Chinese University of Hong Kong, Hong Kong, in 2008. He was a Post-Doctoral Researcher with the Laboratory for Computational Sensing and Robotics and the Engineering, Center for Computer-Integrated Surgical Systems and Technology, Department of Biomedical Engineering and Department of Computer Science, The Johns Hopkins University, Baltimore, MD, USA, from 2008 to 2010. In 2010, he joined the Pediatric Cardiac Biorobotics Laboratory, Department of Cardiovascular Surgery, Children's Hospital Boston and Harvard Medical School, Boston, MA, USA, for investigating the beating heart robotic surgery system. He is currently an Assistant Professor and is leading a research group on medical mechatronics with the Biomedical Engineering Department, National University of Singapore (NUS), Singapore. Prior to joining NUS, he was also with the Surgical Innovation Institute of the Children's National Medical Center, Washington, DC, USA, in 2012, where he was involved in a collaborative computer integrated surgery project.

BOK SENG YEOW received the bachelor's degree from the National University of Singapore. He is a Research Engineer under Prof. H. Ren and conducts the experiments.

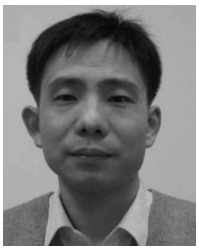

JINJI SUN received the Ph.D. degree in precision instruments and machinery from Beihang University in 2010. He was a Visiting Research Fellow and is a Professor with Beihang University, contributing to the design and fabrication of the needleless injector. He is a Visiting Research Fellow with the Department of Biomedical Engineering, National University of Singapore. His research interests include the design of various types of magnetic actuators.

JAYANT VENKATRAMANI IYER completed the undergraduate medical training at the National University of Singapore in 2004. He is currently a Consultant with the Singapore National Eye Centre and is a Specialist in general ophthalmology and adult cataract surgery, with a special interest in the field of glaucoma; he is the Medical Consultant for this project. He is a Consultant with the Singapore National Eye Centre. He was nominated as the Best House Officer in two of his three rotations. He was awarded the Graduate Diploma in Family Medicine in 2009 and the Master of Medicine (Ophthalmology) in 2011, for which he was awarded the Ministry of Health Post-Graduate Examinations Scholarship. Upon completion of his residency, he became a fellow of the Royal College of Ophthalmologists, U.K., and completed his Fellowship examinations at the Academy of Medicine, Singapore (FAMS), with a Gold Medal in 2014.